

### 3-D Weak Lensing Mass Map Reconstruction: Reducing the line of sight smearing

#### ABSTRACT

A new method is developed to reconstruct 3-D density contrast maps from photometric weak-lensing shear measurements. The 3-D density contrast maps are modeled as a summation of the NFW basis atoms, which have 2-D multi-scale NFW surface density profiles on the transverse plane and 1-D Dirac delta functions in the line of sight direction. With the prior assumption that the density fields have a sparse spatial distribution, the density fields are reconstructed using an oracle algorithm: adaptive lasso. The method is tested with realistic simulations using the HSC-like shape estimation error and photo- $z$  uncertainty. Our findings are summarized as follows: 1) The lasso solution suffers from a smear of structure in the line of sight direction even in the absence of shape noise. In contrast, the adaptive lasso algorithm efficiently removes the line of sight smear of structure. 2) The algorithm is able to detect halo with minimal mass limits of  $10^{14.0}M_{\odot}/h$ ,  $10^{14.7}M_{\odot}/h$ ,  $10^{15.0}M_{\odot}/h$  for the low ( $z < 0.3$ ), median ( $0.3 \leq z < 0.6$ ) and high ( $0.6 \leq z < 0.85$ ) redshifts, respectively, with a false detection of  $0.022/\text{deg}^2$ . 3) The estimated redshift of the halos detected from the reconstructed mass maps are lower than the true redshift by about 0.03 for halos at low redshifts ( $z \leq 0.4$ ). The relative redshift bias is below 0.5% for halos at  $0.4 < z \leq 0.85$ .

#### 1. INTRODUCTION

Weak lensing refers to the phenomenon that light from distant galaxies is distorted by the intervening inhomogeneous density distribution along the line of sight due to gravity's influence. As a result of the light distortion, the shapes of the background galaxies are coherently distorted. The lensing effect imprints the information of foreground mass density distribution to the background galaxy images and offers a direct probe into the mass density distribution in our universe (see Kilbinger 2015; Mandelbaum 2018, for recent reviews).

The expected shear measurements ( $\gamma$ ) on distant galaxies are related to the foreground density contrast field ( $\delta$ ) through a linear transformation:

$$\gamma = \mathbf{T}\delta, \quad (1)$$

where  $\mathbf{T}$  is used to denote the linear transformation operator, which includes not only the physical lensing effect but also systematic effects from observations (e.g., pixelization and smoothing of the shear field in the transverse plane, photo- $z$  uncertainty).

Several large-scale surveys target to study the weak-lensing effect at a high precision level (e.g., HSC (Aihara et al. 2018), KIDS (de Jong et al. 2013), DES (The Dark Energy Survey Collaboration 2005), LSST (LSST Science Collaboration et al. 2009), Euclid (Laureijs et al. 2011), NGRST (Spergel et al. 2015)).

The primary goal of most weak-lensing surveys is to constrain the cosmology model through the 2-point correlations. The studies include galaxy–galaxy lensing,

which cross-correlating the shear field ( $\gamma$ ) with the positions of foreground galaxies (Han et al. 2015; More et al. 2015; Prat et al. 2018), and cosmic shear which auto-correlates the shear measurements (Morrison et al. 2016; Troxel et al. 2018; Hikage et al. 2019; Hamana et al. 2020). Since the shear is directly related to the foreground matter distribution as shown in eq. (1), Galaxy–galaxy lensing probes into the correlation between the matter field and galaxy field. On the other hand, cosmic shear probes into the auto-correlation of matter field.

The reconstruction of density map from shear measurements also receive considerable interest as it reaches the nonlinear scales. The 2-D density map reconstruction which recovers an integration of projected mass along the line of sight has been well studied within the community (Kaiser & Squires 1993; Lanusse et al. 2016; Price et al. 2020) and applied to large-scale surveys (Oguri et al. 2018; Chang et al. 2018; Jeffrey et al. 2018). However, the reconstruction of 3-D mass map is still a challenging task.

To fully reconstruct the 3-D mass density distribution ( $\delta$ ) from the photometric shear observations ( $\gamma$ ), the density contrast field is modeled as a summation of basis atoms in a model dictionary:

$$\delta = \Phi x, \quad (2)$$

where  $\Phi$  is the transformation operator from the projection coefficient field to the density contrast, and  $x$  denotes the projection coefficients. Simon et al. (2009)

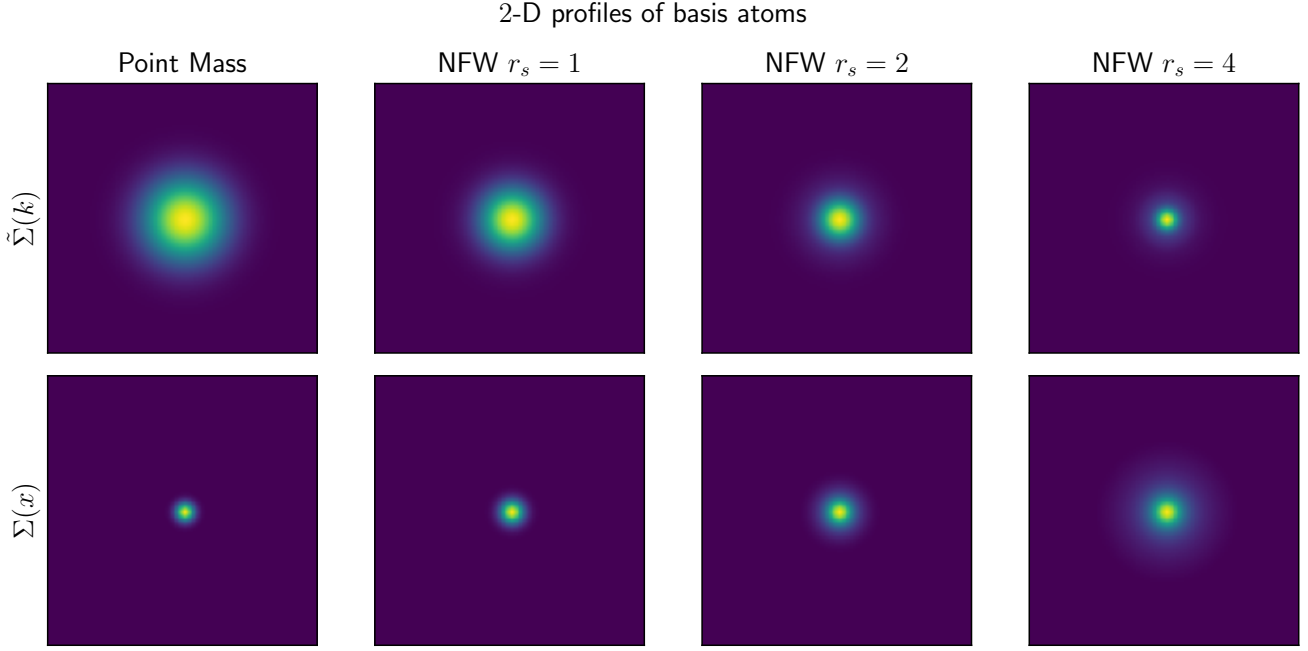


**Figure 1.** The smoothed pixelized basis atoms. The upper row shows the basis atoms in Fourier space, and the lower row shows the basis atoms in Real space. The leftmost column is the point mass atom, and the other columns are the multi-scale NFW atoms. The smoothing kernel is Gaussian with a standard deviation of 1.5 pixels.

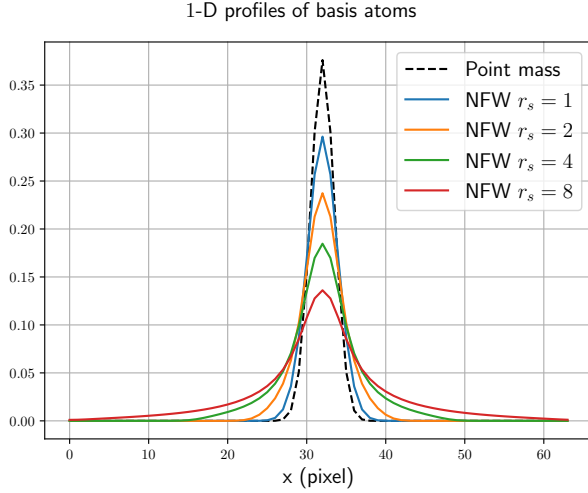


**Figure 2.** The 1-D slices for smoothed pixelized basis atoms at  $x = 0$ . The corresponding 2-D profiles are shown in Figure 1.

reconstruct the density field in Fourier space, which is equivalent to modeling the mass field with sinusoidal functions. On the other hand, Leonard et al. (2014) model the mass field with Starlets (Starck et al. 2015).

The projection coefficients are estimated by optimizing a regularized loss function. The estimator is generally defined as

$$\hat{x} = \arg \min_x \left\{ \frac{1}{2} \left\| \Sigma^{-\frac{1}{2}} (\gamma - \mathbf{T}\Phi x) \right\|_2^2 + \lambda C(x) \right\}, \quad (3)$$

where  $\left\| \Sigma^{-\frac{1}{2}} (\gamma - \mathbf{T}\Phi x) \right\|_2^2$  is the  $l^2$  chi-square term<sup>1</sup> measuring the difference between the prediction and the data, while  $C(x)$  is the regularization term measuring the deviation of the coefficient estimation ( $x$ ) from the prior assumption. The  $l^p$  norm is defined as

$$\|x\|_p = \left( \sum_i |x_i|^p \right)^{\frac{1}{p}}. \quad (4)$$

Such penalized estimation prefers the parameters that are able to describe the observations and align with the prior assumption. The regularization parameter  $\lambda$  adjusts the relative weight between the data and prior assumption in the optimization process.

Simon et al. (2009) propose to use the Wiener filter, which is also known as  $l^2$  ridge regulation ( $C = \|x\|_2^2$ ), to find a regularized solution in Fourier space. Oguri et al. (2018) apply the method of Simon et al. (2009) to the first-year data of the Hyper Suprime-Cam Survey (Aihara et al. 2018). However, the density maps reconstructed by this method suffer from smearing along the line of sight direction with a standard deviation of  $\sigma_z = 0.2 \sim 0.3$ .

Leonard et al. (2014) propose the Glimpse algorithm, which uses a derivative version of  $l^1$  lasso regulation ( $C = \|x\|_1$ ) to find a sparse solution in the Starlet dic-

<sup>1</sup> weighted by the inverse of the diagonal covariance matrix of the error on the shear measurements ( $\Sigma$ ).

tionary space (Starck et al. 2015). Leonard et al. (2014) apply a greedy coordinate descent algorithm, which selects the steepest coordinate in each iteration, to find the minimum of a non-convex loss function penalized with the firm thresholding function. The Glimpse algorithm significantly reduce the smearing along the line of sight. However, the stability of the non-convex optimization and greedy coordinate descent algorithm has not been fully justified. Moreover, the Starlet dictionary are not designed to model the profile of clumpy mass in the universe, and the Starlet dictionary does not account for the angular scale difference at different lens redshifts.

$N$ -body simulations have shown that the dark matter is distributed in halos connected by filaments, and the density profile of a single halo follows the NFW function (Navarro et al. 1997). We construct a model dictionary with the multi-scale NFW atoms. The atoms follow multi-scale surface density profiles of the NFW functions (Takada & Jain 2003) on the transverse plane. Following Leonard et al. (2014), we neglect the depth of halos since the resolution scale of the reconstruction in the line of sight direction is much larger than the halo scale. Therefore, we set the NFW atoms' profile in the line of sight direction as the Dirac delta function. Moreover, we assume that the halos are sparsely distributed in the universe. With the sparsity prior, the adaptive lasso regularization (Zou 2006) is used to reconstruct the density field. We find that, in contrast to the lasso estimator that smears the structure along the line of sight, the adaptive lasso can significantly reduce the smearing effect.

Compared with Leonard et al. (2014), our dictionary is built up to describe the clumpy mass in the universe with a clear physical motivation. Furthermore, the adaptive lasso algorithm is strictly convex and can be directly optimized with the FISTA algorithm (Beck & Teboulle 2009) without relying on any greedy coordinate descent approaches. The stability of this convex optimization has been well studied.

This paper is organized as follows. In Section 2, we propose the new method for 3-D density map reconstruction. In Section 3, we test the novel algorithm on HSC-like simulations. In Section 4, we summarize and discuss the future development of the method.

## 2. METHODOLOGY

We first review the lensing process in Section 2.1. Then, we introduce the dictionary used to model the foreground density maps in Section 2.2.

Subsequently, in Section 2.3, we discuss several systematic effects from observations which include photo- $z$

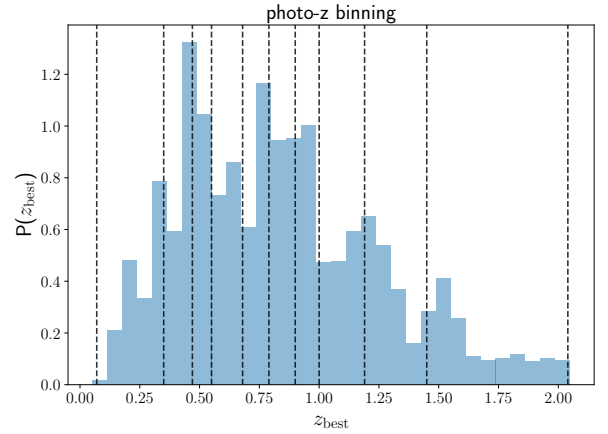


**Figure 3.** The source galaxies are binned into 10 redshift bins according to their Machine Learning and photo-Z (MLZ) best photo- $z$  estimation. The blue histogram is the normalized number distribution of the best photo- $z$  estimation. The vertical dashed lines are the boundaries of the redshift bins. The galaxies are equal-number binned.

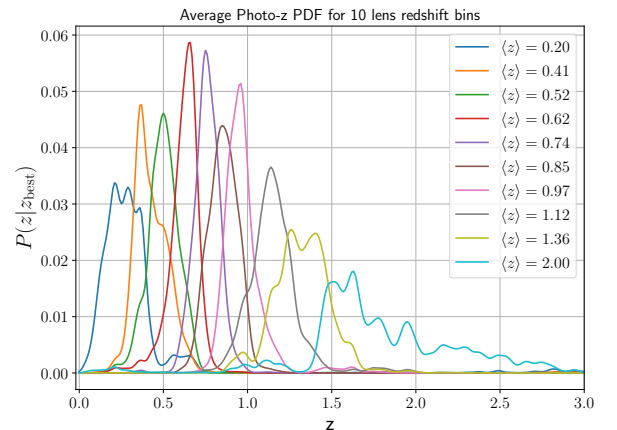


**Figure 4.** The average PDF of MLZ photo- $z$  error for 10 source redshift bins.

uncertainty (Section 2.3.1), smoothing (Section 2.3.2), masking (Section 2.3.3), and pixelization (Section 2.3.4).

Finally, we solve the mass reconstruction problem in Section 2.4 using the adaptive lasso algorithm (Zou 2006) optimized with the FISTA algorithm (Beck & Teboulle 2009).

### 2.1. Lensing

The lensing convergence map at the comoving distance  $\chi_s$  caused by the foreground inhomogeneous density distribution at the comoving distance  $\chi_l$  ( $\chi_l < \chi_s$ ) along the line of sight is

$$\kappa(\vec{\theta}, \chi_s) = \frac{3H_0^2\Omega_M}{2c^2} \int_0^{\chi_s} d\chi_l \frac{\chi_l \chi_{sl}}{\chi_s} \frac{\delta(\vec{\theta}, \chi_l)}{a(\chi_l)}, \quad (5)$$

where  $\delta = \rho(\vec{\theta}, \chi_l)/\bar{\rho} - 1$  is the density contrast at the position of lens,  $H_0$  is the Hubble parameter,  $\Omega_M$  is the matter density parameter,  $c$  is the speed of light, and  $a(\chi_l)$  is the scale parameter at the lens position.

After substituting comoving distance ( $\chi$ ) with redshift ( $z$ ), we have

$$\kappa(\vec{\theta}, z_s) = \int_0^{z_s} dz_l K(z_l, z_s) \delta(\vec{\theta}, z_l). \quad (6)$$

where  $K(z_l, z_s)$  is the lensing kernel defined as

$$K(z_l, z_s) = \begin{cases} \frac{3H_0\Omega_M}{2c} \frac{\chi_l \chi_{sl}(1+z_l)}{\chi_s E(z_l)} & (z_s > z_l), \\ 0 & (z_s \leq z_l), \end{cases} \quad (7)$$

where  $E(z)$  is the Hubble parameter as a function of redshift, in units of  $H_0$ .

As shown in Kaiser & Squires (1993), the shear field is related to the kappa field at the same redshift plane via

$$\gamma_L(\vec{\theta}, z_s) = \int d^2\theta' D(\vec{\theta} - \vec{\theta}') \kappa(\vec{\theta}', z_s), \quad (8)$$

where

$$D(\vec{\theta}) = -\frac{1}{\pi} (\theta_1 - i\theta_2)^{-2}. \quad (9)$$

Here we denote the physical shear distortion field as  $\gamma_L$  and we note that the final observed shear measurements are influenced by systematic errors from observations. The systematic errors will be discussed in Section 2.3.

Combining equation (6) with equation (8), the expectation of lensing shear signal is

$$\gamma_L(\vec{\theta}, z_s) = \int_0^{z_s} dz_l K(z_l, z_s) \int d^2\theta' \vec{D}(\vec{\theta} - \vec{\theta}') \delta(\vec{\theta}', z_l). \quad (10)$$

To simplify the expression, we define the lensing transform operator as

$$\mathbf{Q} = \int_0^{z_s} dz_l K(z_l, z_s) \int d^2\theta' \vec{D}(\vec{\theta} - \vec{\theta}'), \quad (11)$$

and eq. (10) is simplified to

$$\gamma_L = \mathbf{Q}\delta. \quad (12)$$

## 2.2. Dictionary

The density contrast field is modeled as a summation of basis atoms in the dictionary:

$$\delta(\vec{r}) = \sum_{s=1}^N \int d^3r' \phi_s(\vec{r} - \vec{r}') x_s(\vec{r}'), \quad (13)$$

where  $\phi_s(\vec{r})$  are the basis atoms of the dictionary. The basis atoms have ‘ $N$ ’ different scale frames, and the

atoms in each scale frame are shifted by  $\vec{r}'$  to form models at different spatial positions.  $x_s(\vec{r}')$  is the projection coefficients of the density contrast field onto the basis atoms.

We propose to use the multi-scale NFW atoms, denoted as  $\{\phi_1, \dots, \phi_N\}$ , as the basis atoms of our dictionary. On the transverse plane, the NFW atoms follow surface density profiles of the NFW halos (Takada & Jain 2003) with scale radius  $\theta_\alpha$  and truncation radius  $c\theta_\alpha$ , where  $c$  is the concentration of the NFW halos. As the scales of halos are much smaller than the reachable redshift resolution, we neglect the depth of halo on the line of sight direction and set the NFW atoms’ profiles in the line of sight direction to 1-D Dirac delta functions as suggested by (Leonard et al. 2014). The multi-scale NFW atoms are defined as

$$\phi_\alpha(\vec{r}) = \frac{f}{2\pi\theta_\alpha^2} F(|\vec{\theta}|/\theta_\alpha) \delta_D(z), \quad (14)$$

( $s = 1..N$ )

where

$$F(x) = \begin{cases} -\frac{\sqrt{c^2-x^2}}{(1-x^2)(1+c)} + \frac{\text{arccosh}\left(\frac{x^2+c}{x(1+c)}\right)}{(1-x^2)^{3/2}} & (x < 1), \\ \frac{\sqrt{c^2-1}}{3(1+c)} \left(1 + \frac{1}{c+1}\right) & (x = 1), \\ -\frac{\sqrt{c^2-x^2}}{(1-x^2)(1+c)} + \frac{\arccos\left(\frac{x^2+c}{x(1+c)}\right)}{(x^2-1)^{3/2}} & (1 < x \leq c), \\ 0 & (x > c). \end{cases} \quad (15)$$

$f = 1/[\ln(1+c) - c/(1+c)]$ . In this work, we fix  $c = 4$  for the NFW atoms in different scale frames.

To simplify the notation, we compress the projection

coefficients into a column vector:  $x = \begin{pmatrix} x_0 \\ x_1 \\ \dots \\ x_N \end{pmatrix}$ , and com-

press the dictionary transform operator to a row vector:

$$\Phi = \left( \int d^3r \phi_0(\vec{r}) \int d^3r \phi_1(\vec{r}) \dots \int d^3r \phi_N(\vec{r}) \right). \quad (16)$$

We substitute eq. (13) into eq. (10) and get

$$\gamma_L = \mathbf{Q}\Phi x. \quad (17)$$

In this paper, a dictionary constructed with point mass atoms is used to compare with the dictionary of multi-scale atoms. The point mass atoms is a 3-D Dirac function defined as follows

$$\phi_{\text{PM}}(\vec{r}) = \delta_D(\theta_1) \delta_D(\theta_2) \delta_D(z). \quad (18)$$



**Figure 5.** The left panel shows the lensing kernels for five different lens redshifts. The dashed lines are the kernels for spectroscopic redshift, which assumes that the source galaxies’ redshifts are precisely estimated. The solid lines are for photometric redshifts, which accounts for the influence of photometric redshift uncertainty. The other two panels show the correlation between lensing kernels of different lens redshifts. The middle panel is for spectroscopic redshift, and the right panel is for photometric redshifts. The lensing kernels are normalized so that the diagonal elements of the correlation matrices equal one.

The 2-D profiles of the point mass atom and the multi-scale NFW atoms on the transverse plane are shown in Figure 1. The 1-D slices of the profiles are demonstrated in Figure 2. Note that these profiles are smoothed with a Gaussian kernel and pixelized into evenly spaced grids. The smoothing operation is discussed in Section 2.3.2, and the pixelization operation is discussed in Section 2.3.4.

### 2.3. Systematics

The observed shear measurements are deviated from the physical shear prediction due to the systematic errors from observations. The influence of systematics is carefully studied and incorporated into the forward modeling in this Section.

#### 2.3.1. Photo- $z$ Uncertainty

The photometric redshifts of source galaxies in the current large-scale survey are estimated with a limited number of board photometric bands (e.g., 9 bands for KIDS+VIKING survey (Hildebrandt et al. 2020), 5 bands for DES survey and HSC survey). As a result, the estimated redshifts of galaxies suffer from much larger uncertainties than redshifts estimated with spectroscopic observations. Such photo- $z$  uncertainty smears the lensing kernels statistically since a galaxy with a best fit photo- $z$  estimation of  $z_s$  has possibilities of being actually located at different redshifts ( $z$ ). The probability function for the photo- $z$  uncertainty is denoted as  $P(z|z_s)$ , and the expected shear distortion on the galaxy is

$$\int dz_s P(z|z_s) \gamma_L(\vec{\theta}, z_s). \quad (19)$$

With the definition of photo- $z$  smearing operator:

$$\mathbf{P} = \int dz_s P(z|z_s), \quad (20)$$

the photo- $z$  uncertainty changes the shear as

$$\gamma_L \rightarrow \mathbf{P} \gamma_L, \quad (21)$$

where we use  $\rightarrow$  to denote the changes of shear by the systematic operator.

Figure 3 shows the histogram of the best Machine Learning and photo- $z$  (Carrasco Kind & Brunner 2013, MLZ) photometric redshift estimation from Tanaka et al. (2018) for galaxies in the tract 9347 of the HSC S16A data release (Aihara et al. 2018). These Galaxies are divided into ten source galaxy bins according to the photo- $z$  best estimation, and the boundaries of the bins are shown as vertical dashed lines in Figure 3. Figure 4 shows the average probability density function (PDF) for galaxies in each redshift bin.

The left panel of Figure 5 shows the lensing kernels for lenses at five different redshifts as functions of source galaxy redshift bins. The dashed lines are the lensing kernel for spectroscopic redshifts with neglectable redshift uncertainty. The solid lines are the lensing kernel for photometric redshifts with redshift uncertainties shown in Figure 4. As shown by the dashed lines in the left panel of Figure 5, the lensing kernels converge to zero for source redshifts lower than the lens redshift if the uncertainties on the source galaxy redshift estimations are neglectable. However, as demonstrated by the solid lines in the same panel, for the source redshifts with large photo- $z$  uncertainties, the lensing kernels do not converge to zero at redshifts lower than the lens redshift. This is because the galaxies with photo- $z$  estimations lower than the lens redshifts may be actually located at higher redshifts due to the photo- $z$  uncertainties.

The middle and right panels show the correlation between lensing kernels for lenses at different redshifts. The middle panel is for spec- $z$ , and the right panel is

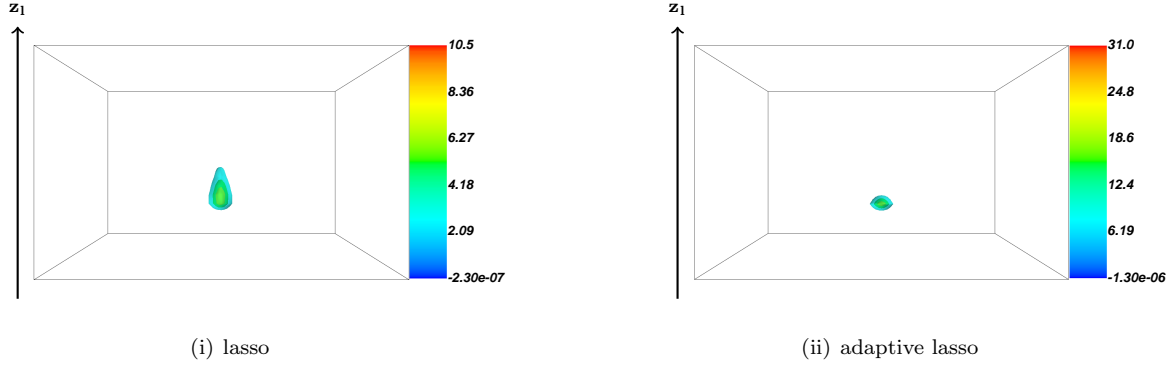


**Figure 6.** The density map reconstructions with the lasso (left) and the adaptive lasso (right) algorithms. The vertical direction is the line of sight direction, and the lower boundaries and upper boundaries of the boxes are  $z = 0.01$  and  $z = 0.85$ , respectively. Noises on galaxy shape measurements are neglected in the simulation. The input halo mass is  $M_{200} = 10^{15} h^{-1} M_{\odot}$ , and its redshift is  $z = 0.35$ . The lasso reconstruction smears the density field along the line of sight direction.

for photo- $z$ . As demonstrated in the middle panel, the lensing kernels are highly correlated even though the redshift estimation is precise. Comparing the correlation matrices shown in the middle panel and the right panel of Figure 5, we conclude that the photo- $z$  uncertainties further increase the correlations between lensing kernels at different lens plane.

### 2.3.2. Smoothing

The observed galaxies have random yet unequally-spaced spatial distribution. To boost the computational speed, we smooth the shear measurements from galaxy shapes and pixelize the smoothed measurements onto regular grids. After the pixelization, the fast Fourier transform (FFT) can be directly conducted on the transverse plane in each source redshift bin.

The smoothing is conducted by convolving the shear measurements with a smoothing kernel:

$$\gamma_{\text{sm}}(\vec{\theta}) = \frac{\sum_i W(\vec{\theta} - \vec{\theta}_i, z - z_i) \gamma_i}{\sum_i W(\vec{\theta} - \vec{\theta}_i, z - z_i)}, \quad (22)$$

where  $W(\vec{\theta}, z)$  is a 3-D smoothing kernel.  $\gamma_i$ ,  $z_i$  and  $\theta_i$  are the shear, photometric redshift, and transverse position of the  $i$ -th galaxy in the catalog.

$W(\vec{\theta}, z)$  can be decomposed into a transverse component  $W_T(\vec{\theta})$  and a line of sight component  $W_{\times}(z)$  as

$$W(\vec{\theta}, z) = W_T(\vec{\theta}) W_{\times}(z). \quad (23)$$

In this paper, we use an isotropic 2-D Gaussian kernel and a 1-D top-hat kernel to smooth the measurements in the transverse plane and the line of sight direction.

These components of the smoothing kernel are

$$W_T(\vec{\theta}) = \frac{1}{2\pi\beta^2} \exp\left(-\frac{|\vec{\theta}|^2}{2\beta^2}\right), \quad (24)$$

$$W_{\times}(z) = \begin{cases} 1/\Delta z & (|z| < \Delta z/2), \\ 0 & \text{else.} \end{cases}$$

In this paper, we set  $\beta = 1.5$ .

Since the smoothing kernel is normalized by definition:

$$\int d^3r W(\vec{r}) = 1, \quad (25)$$

with the approximation that the density of galaxy number -  $n(\vec{r})$  - varies slowly at the smoothing scale, the smoothed galaxy number density:

$$n_{\text{sm}}(\vec{r}) = \sum_i W(\vec{r} - \vec{\theta}_i, z - z_i), \quad (26)$$

equals the galaxy number density:  $n_{\text{sm}}(\vec{r}) = n(\vec{r})$ . We note that the galaxy number density experience a steep drop on the boundary of the survey, therefore the smoothed galaxy number density does not equal the galaxy number density close to the boundary of the survey.

The smoothing operator is defined as

$$\mathbf{W} = \int d^3r' W(\vec{r} - \vec{r}'), \quad (27)$$

and the smoothing procedure influence the shear signal through

$$\gamma_L \rightarrow \mathbf{W} \gamma_L. \quad (28)$$

As we will discuss in Section 2.3.4, the smoothed shear field is pixelized into equally spaced grids. We note that another widely used scheme is to average the shear measurements in each pixel. Such a scenario is equivalent to resampling the shear field smoothed with a 3-D top-hat kernel with the same scale as the pixels.



### 2.3.3. Masking

In real observations, shear measurements are available in a finite region of the sky, and the boundary of the region is always irregular. Moreover, many isolated sub-regions near the bright stars are masked out since the light from bright stars tends to influence the shear measurements on neighboring galaxies.

We define the masking window function according to the smoothed number density (defined in eq. (26)) of the galaxies:

$$M(\vec{r}) = \begin{cases} 0 & n_{\text{sm}} > 1, \\ 1 & \text{else.} \end{cases} \quad (29)$$

The mask changes the shear measurements though

$$\gamma_L(\vec{\theta}, z) \rightarrow M(\vec{\theta}, z) \gamma_L(\vec{\theta}, z), \quad (30)$$

We define the masking operator as

$$\mathbf{M} = \int d^3 r' M(\vec{r}') \delta_D(\vec{r} - \vec{r}'), \quad (31)$$

where  $\delta_D(\vec{r})$  is 3-D Dirac delta function. The shear is influenced by the masking by  $\gamma_L \rightarrow \mathbf{M} \gamma_L$ .

The final observed shear field, taking into account all of the systematics as mentioned above from observations, is

$$\gamma = \mathbf{MWPQ}\Phi x. \quad (32)$$

For simplicity, we denote  $\mathbf{A} = \mathbf{MWPQ}\Phi$  and eq. (32) is written as

$$\gamma = \mathbf{A}x. \quad (33)$$

### 2.3.4. Pixelization

We pixelize the smoothed shear field into an  $N_\theta \times N_\theta \times N_s$  grid, where  $N_\theta$  is the number of pixels for the two orthogonal axes of the transverse plane and  $N_s$  is the number of pixels for the line of sight axis.  $\gamma_\alpha$  denotes the smoothed shear measurements recorded on the pixel with index  $\alpha$ , where  $\alpha = 1 \dots N_\theta \times N_\theta \times N_s$ . The grids on the transverse planes are equally spaced with a pixel size of  $1'$ . Fast Fourier transform (FFT) can be used to boost the speed of linear operation on the transverse plane, whereas the grids in the line of sight direction follow equal number binning as shown in Figure 3.

Similarly, we pixelize each scale frame of the projection coefficient field  $x$  into an  $N_\theta \times N_\theta \times N_l$  grid. The pixelization on the transverse plane for each scale frame is the same as that of the smoothed shear field on the transverse plane. At the same time, the projection coefficient field is pixelized into equal spaced grids in the line of sight direction ranging from redshift 0.01 to redshift 0.85. Here, we use  $N_l$  to denote the number of the

lens planes and  $x_\beta$  to denote the projection parameter indexed as  $\beta$ , where  $\beta = 1 \dots N_\theta \times N_\theta \times N_l \times N$ . The corresponding pixelized elements of the forward transform matrix  $\mathbf{A}$  is denoted as  $A_{\alpha\beta}$ .

We term the column vectors of the forward transform matrix  $\mathbf{A}$  as the effective basis atoms. We note that the effective basis atoms have different  $l^2$  norm. The  $l^2$  norm of the  $i$ 'th column vectors of the effective basis atoms are  $\mathcal{N}_i = \sum_\alpha A_{i\alpha} A_{i\alpha}$ . Before solving the density map reconstruction problem, we normalize the column vectors of the transform matrix through a rescaling:

$$\begin{aligned} A'_{\alpha\beta} &= A_{\alpha\beta} / \mathcal{N}_\alpha^{\frac{1}{2}}, \\ x'_\beta &= x_\beta \mathcal{N}_\beta^{\frac{1}{2}}. \end{aligned} \quad (34)$$

## 2.4. Density map reconstruction

### 2.4.1. Adaptive lasso

The lasso algorithm uses  $l^1$  norm of the projection coefficient field to regularize the modeling, and the estimator is defined as

$$\hat{x}'^{\text{lasso}} = \arg \min_x \left\{ \frac{1}{2} \left\| \Sigma^{-\frac{1}{2}} (\gamma - \mathbf{A}' x') \right\|_2^2 + \lambda \|x'\|_1 \right\}, \quad (35)$$

where  $\|\cdot\|_1$  and  $\|\cdot\|_2$  refer to the  $l^1$  norm and  $l^2$  norm, respectively.  $\lambda$  denotes the penalization parameter for the lasso estimation.

The lasso algorithm selects the parameters relevant to the measurements and simultaneously estimates the value of the selected parameters. However, it has been shown by Zou (2006) that when the column vectors of the transforming matrix  $\mathbf{A}'$  are highly correlated, the lasso cannot select the relevant parameters from the parameter space consistently. Moreover, the estimated parameters are biased due to the shrinkage in the lasso regression. We note that, for the density map reconstruction problem, the column vectors are highly correlated even in the absence of photometric redshift uncertainties because, as shown in Figure 5, the lensing kernels for lenses at different redshifts are highly correlated. Therefore, the lasso algorithm cannot select the consistent mass in the line of sight direction, and the reconstructed mass suffers from smears in the line of sight direction even in the absence of noise on shear measurements. Figure 6 shows the reconstructions of a single halo's mass map with halo mass equals  $M_{200} = 10^{15} h^{-1} M_\odot$  at redshift 0.35. The noises on shear measurements are not included in the simulation. The left panel of Figure 6 is the reconstruction with the lasso algorithm, which shows a significant smear along the line of sight.

Zou (2006) proposes the adaptive lasso algorithm, which uses adaptive weights to penalize different projection coefficients in the  $l^1$  penalty. The adaptive lasso

algorithm is a two-steps process. In the first step, the lasso is used to estimate the parameters, and the preliminary estimation of the lasso is denoted as  $\hat{x}'^{\text{lasso}}$ . In the second step, the preliminary lasso estimation is used to weight the penalization. The weight on penalty is defined as

$$\hat{w} = \frac{1}{\left| \hat{x}'^{\text{lasso}} \right|^\tau}, \quad (36)$$

where we set the hyper-parameter  $\tau$  to 2. The adaptive lasso estimator is expressed as

$$\hat{x}' = \arg \min_{x'} \left\{ \frac{1}{2} \left\| \Sigma^{-\frac{1}{2}} (\gamma - \mathbf{A}' x') \right\|_2^2 + \hat{w} \lambda_{\text{ada}} \|x'\|_1 \right\}. \quad (37)$$

Here,  $\lambda_{\text{ada}}$  is the penalization parameter for the adaptive lasso. We note that  $\lambda_{\text{ada}}$  does not need to be the same as the penalization parameter for the preliminary lasso estimation ( $\lambda$ ).

We rewrite the loss function with the Einstein notation:

$$L(x') = \frac{1}{2} (\Sigma^{-1})_{\alpha\beta} (\gamma_\alpha^* - A'_{\alpha i} x'_i) (\gamma_\beta - A'_{\beta j} x'_j) + \lambda_{\text{ada}} \hat{w}_\beta |x'_\beta|. \quad (38)$$

To simplify the notation in future, we define the quadruple term in the loss function as  $G(x')$ :

$$G(x') = \frac{1}{2} \Sigma_{\alpha\beta}^{-1} (\gamma_\alpha^* - A'_{\alpha i} x'_i) (\gamma_\beta - A'_{\beta j} x'_j). \quad (39)$$

#### 2.4.2. FISTA

Beck & Teboulle (2009) propose the Fast Iterative Soft Thresholding Algorithm (FISTA) to solve the lasso problem. Since the lasso's loss function and the adaptive lasso's loss function only differ in their penalization terms. The FISTA is also applicable to the adaptive lasso problem. We apply the FISTA to solve both the preliminary lasso estimation and the final adaptive lasso estimation.

Here we start from the lasso preliminary estimation. The coefficients are initialized as  $x_i^{(1)} = 0$ . According to the FISTA algorithm, we iteratively update the projection coefficient field ( $x$ ). Taking the  $n$ 'th iteration as an example, a temporary update is first calculated as

$$x_i'^{(n+1)} = \text{ST}_\lambda \left( x_i'^{(n)} - \mu \partial_i G(x'^{(n)}) \right), \quad (40)$$

where ST is the soft thresholding function defined as

$$\text{ST}_\lambda(x') = \text{sign}(x') \max(|x'| - \lambda, 0). \quad (41)$$

The soft thresholding is a part of the lasso algorithm. It selects the estimations with amplitude larger than  $\lambda$ ,

and shrink the estimations by  $\lambda$ .  $\mu$  is the step size of the gradient descent iteration.  $\partial_i G(x'^{(n)})$  refers to the  $i$ 'th element of the gradient vector of  $G$  at point  $x'^{(n)}$ :

$$\partial_i G(x'^{(n)}) = \Sigma_{\alpha\beta}^{-1} \text{Re} \left( A'_{\alpha i}^* (\gamma_\beta - A'_{\beta j} x'_j) \right), \quad (42)$$

where  $\text{Re}(\bullet)$  is the function returns the real part of the input function. The FISTA algorithm requires an additional update amounting to a weighted average between  $x'^{(n+1)}$  and  $x'^{(n)}$ :

$$t^{(n+1)} = \frac{1 + \sqrt{1 + 4(t^{(n)})^2}}{2}, \quad (43)$$

$$x'^{(n+1)} \leftarrow x'^{(x+1)} + \frac{t^{(n)} - 1}{t^{(n+1)}} (x'^{(n+1)} - x'^{(n)}),$$

where the relative weight is initialized as  $t^{(1)} = 1$ .

The FISTA algorithm converges as long as the gradient descent step size  $\mu$  satisfies

$$0 < \mu < \frac{1}{\|\mathbf{A}^\dagger \Sigma^{-1} \mathbf{A}\|}, \quad (44)$$

where  $\|\mathbf{A}^\dagger \Sigma^{-1} \mathbf{A}\|$  refers to the spectrum norm of the matrix  $\mathbf{A}^\dagger \Sigma^{-1} \mathbf{A}$ . The spectral norm is estimated by simulating a large number of random vectors with  $l^2$  norms equal one with different realizations. The matrix operator  $\mathbf{A}^\dagger \Sigma^{-1} \mathbf{A}$  is subsequently applied to each random vector and get a corresponding transformed vector. The spectral norm of the matrix  $\mathbf{A}^\dagger \Sigma^{-1} \mathbf{A}$  is determined as the maximum  $l^2$  norm of the transformed vectors.

As summarized in Algorithm 2.4.2, we first initial the projection coefficients as zero and use the FISTA algorithm to find the global minimum of the lasso loss function. Such a global minimum is the preliminary estimation. We then use the preliminary lasso estimation to weight the coefficients and construct the adaptive lasso loss function. Finally, we set the preliminary lasso estimation as the warm start of the adaptive lasso estimation and use the FISTA algorithm again to find the adaptive lasso loss function's global minimum, which is the final solution.



---

**Algorithm** Our Algorithm
 

---

**Input:**  $\gamma$ : Pixelized complex 3-D array of shear

**Output:**  $\delta$ : 3-D array of density contrast

```

1: Normalize column vectors of  $\mathbf{A}$ 
2: Estimate step size  $\mu$  and  $\Sigma$ 
3: Initialization:
4:  $x^{(1)} = 0$ 
5:  $\hat{w} = 1$ 
6:  $t^{(1)} = 1, i = 1, j = 1$ 
7: while  $j \leq 2$  do
8:   while  $i \leq N_{\text{iter}}$  do
9:     # soft thresholding
10:     $x_i'^{(n+1)} = \text{ST}_{\hat{w}\lambda} \left( x_i'^{(n)} - \mu \partial_i G(x'^{(n)}) \right)$ 
11:    # FISTA algorithm
12:     $t^{(n+1)} = \frac{1 + \sqrt{1 + 4(t^{(n)})^2}}{2}$ 
13:     $x'^{(n+1)} \leftarrow x'^{(n+1)} + \frac{t^{(n)} - 1}{t^{(n+1)}} (x'^{(n+1)} - x'^{(n)})$ 
14:     $i = i + 1$ 
15:   end while
16:   Reinitialization:
17:    $\hat{w} = \left| \hat{x}'^{\text{lasso}} \right|^{-2}, \lambda \leftarrow \lambda_{\text{ada}}$ 
18:    $\hat{x}'^{(1)} = x'^{(N_{\text{iter}})}$ 
19:    $t^{(1)} = 1, i = 1$ 
20:    $j = j + 1$ 
21: end while
22:  $\delta = \Phi \mathcal{N}^{-\frac{1}{2}} x'^{(N_{\text{iter}})}$ 

```

---

### 3. TESTS

This Section simulates weak-lensing shear fields induced by a group of NFW halos with various halo masses and redshifts. The shear fields are used to distort the HSC mock shape catalogs with different realizations of the HSC-like shape measurement errors and photo- $z$  uncertainties (Section 3.1).

Then, we test our algorithm using the simulations with different setups of the regularization parameter. We also compare the results of our algorithm, which uses the NFW dictionary (Section 3.2), with the point mass dictionary (Section 3.3).

#### 3.1. Simulations

The  $\Lambda$ CDM cosmology used in this paper is from the best-fit result of the final full-mission Planck observation of the cosmic microwave background (CMB) with  $H_0 = 67.4 \text{ km s}^{-1} \text{ Mpc}^{-1}$ ,  $\Omega_M = 0.315$ ,  $\Omega_\Lambda = 0.685$  (Planck Collaboration et al. 2020).

We sample halos in a two-dimensional redshift-mass plane. The redshift-mass plane is evenly divided into eight redshift bins and eight mass bins. We randomly shift the input halo redshifts and halo masses from the bins' centers by a small amount. The concentration of the NFW halo is set as a function of the halo's mass ( $M_{200}$ ) and redshift ( $z_h$ ) according to Ragagnin et al.

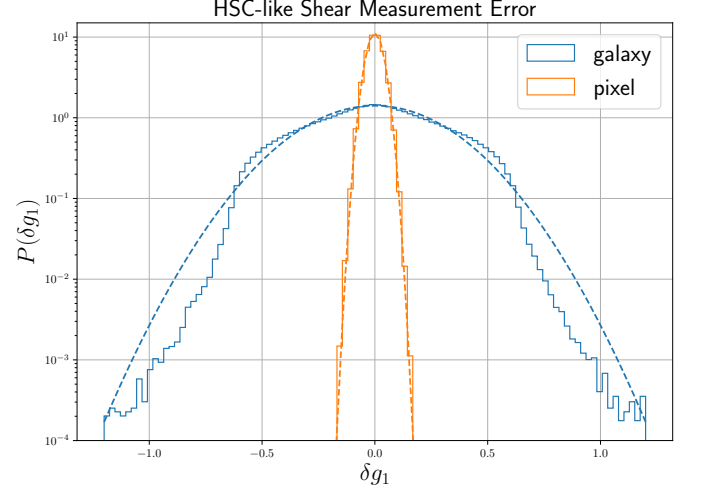


**Figure 7.** The solid lines show the histograms of the HSC-like shape measurement error (including both from shape noise and photon noise) on the first component of shear ( $g_1$ ) for galaxies (blue lines) and smoothed pixels (orange lines). The dashed lines are the best-fit Gaussian distributions to the corresponding histograms.

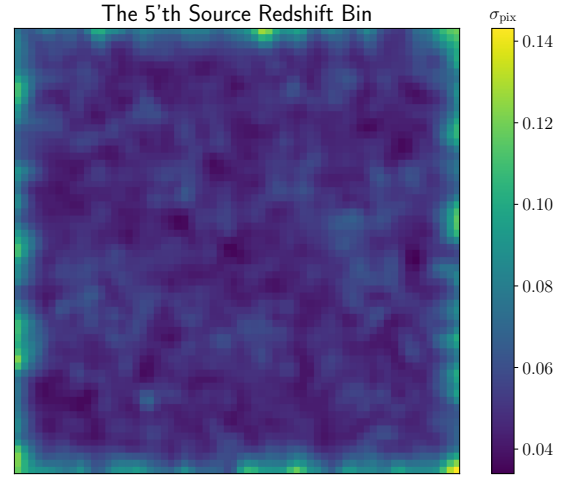


**Figure 8.** The standard deviation pixel map of the HSC-like shape measurement error for the fifth source galaxy bin ( $0.69 \leq z < 0.80$ ).

(2019)

$$c_h = 6.02 \times \left( \frac{M_{200}}{10^{13} M_\odot} \right)^{-0.12} \left( \frac{1.47}{1. + z_h} \right)^{0.16}. \quad (45)$$

The weak-lensing shear fields of these NFW halos are simulated according to Takada & Jain (2003). The shear distortions are applied to one hundred realizations of galaxy catalogs with the HSC-like shape measurement error and photo- $z$  uncertainty.

The mock galaxy catalogs are generated using the HSC S16A shape catalog (Mandelbaum et al. 2018). We use the galaxies in a one square degree region at the center of tract 9347 (Aihara et al. 2018). The galaxies' positions are randomized to distribute homogeneously in the one-square degree stamp statistically. We randomly assign its redshift for each galaxy following the MLZ photo- $z$  probability distribution function (Tanaka et al. 2018).

By randomly rotating the galaxies in the shape catalog, we simulate the HSC-like shape estimation errors with different realizations. The histogram of the first component of the HSC-like shape estimation error on galaxy level is shown in Figure 7. The corresponding histogram of the shape measurement error on the pixel level after the smoothing and pixelization is also shown in 7. The standard deviation map of the noise is demonstrated in Figure 8. As demonstrated in Figure 7, even though the shape measurement error on the galaxy level does not fully follow Gaussian distribution, the error is well described by Gaussian distribution after the smoothing and pixelization.

### 3.2. NFW atoms

In this subsection, we test the performance of our algorithm with the default setup that models the matter density field with multi-scale NFW atoms. The dictionary is constructed with three frames of different NFW scale radii in the comoving coordinate:  $0.12 h^{-1}$  Mpc,  $0.24 h^{-1}$  Mpc, and  $0.36 h^{-1}$  Mpc. The truncation radii are set to four times the comoving scale radii for the atoms in the dictionary (concentration equals four). We note that each frame of our dictionary fixes the scale radius in the comoving space; therefore, the NFW atoms have different angular radii in different lens redshift bins.

We test the algorithm with different regularization parameters ( $\lambda$ ) for the preliminary lasso estimation, which are 3.5, 4.0, and 5.0. The corresponding regularization parameters for the final adaptive lasso estimations are set to  $\lambda_{\text{ada}} = \lambda^{\tau+1}$ . Here, we note that both the preliminary lasso estimation and the final adaptive lasso estimation select the pixels with the signal-to-noise ratios (SNRs) greater than  $\lambda$  in each gradient descent iteration. While the final adaptive lasso estimation further enhances the growth of the pixels with preliminary estimations greater than  $\lambda$ .

This paper does not go beyond the resolution limit defined by the Gaussian smoothing kernel with a standard deviation of  $1.5'$  and the  $1'$  pixel scale as discussed in Section 2.3.2 and Section 2.3.4, respectively. Therefore, we smooth the reconstructed density with the same Gaussian kernel in each lens redshift plane.

Figure 9 shows the 3-D density maps reconstructed with different penalization parameters for a halo with  $M_{200} = 10^{15.02} h^{-1} M_{\odot}$  at redshift 0.164. As we can see from the reconstructed density maps, the adaptive lasso algorithm sets most of the reconstructed pixels to zero and only keeps the pixels with large amplitudes. We identify the peaks on the reconstructed sparse density map.

Following Lanusse et al. (2016), we normalize the detected peaks in the  $l$ -th ( $l = 1 \dots 20$ ) lens redshift plane to account for the peak amplitude difference due to the difference in the norm of the lensing kernels for different redshift bins:

$$\delta_{\text{peak}}^n(\vec{\theta}, z_l) = \delta_{\text{peak}}(\vec{\theta}, z_l) / \mathcal{R}_l^{\frac{1}{2}}, \quad (46)$$

where the normalization matrix is defined as

$$\mathcal{R}_l = \sum_s K^2(z_l, z_s). \quad (47)$$

The solid steps in Figure 10 show the histograms of the normalized peaks with different penalization parameters. Also, we simulate 1000 realizations of pure noise catalogs and perform the reconstructions on these noise catalogs to study the noise properties. The dashed steps in Figure 10 show the histograms of normalized peaks detected from the pure noise catalogs. The solid lines in Figure 10 show the best-fit Gaussian distributions to the noise peaks' histograms.

Figure 10 tells that the densities of peaks (including both true and false peaks) are suppressed as the penalization parameter  $\lambda$  increases. Moreover, we find the standard deviation of noise peaks slightly decreases as  $\lambda$  increases. As a result, for a higher detection threshold ( $\lambda = 5.0$ ), we find a clearer peak number excess for mass maps reconstructed from mock catalogs comparing with the noise peak histogram.

The 2-D histogram, stacked from all of the simulations, for the offsets of the detected peak positions from the input halos' positions is shown in the left panel of Figure 11. We see a clustering of peaks close to the input halo's position on the stacked position histogram. For each stamp simulation, we find the positive peak closest to the input position (in the pixel unit). If the closest peak lay inside the region denoted with the dashed box in the left panel of Figure 11, we take it as a true peak detection of the input halo. Other identified peaks, which include both positive and negative peaks, are taken as false detections.

The right panel of Figure 11 shows the average redshift of true detections for each halo. The estimated redshifts are lower than the true redshifts by about 0.03 for halos in the low-redshift range ( $z \leq 0.4$ ). For halos at  $0.4 < z \leq 0.85$ , the relative redshift bias is below 0.5%.

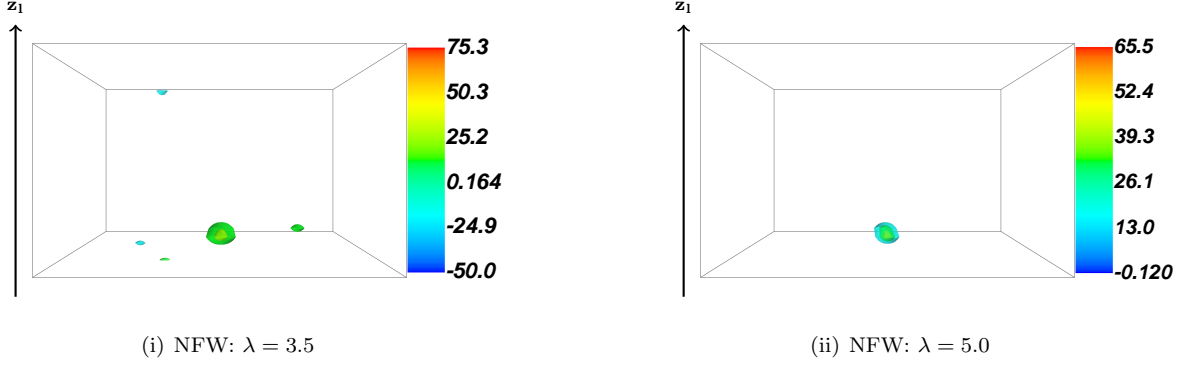


**Figure 9.** The density maps reconstructed from the mock galaxy shape catalog with the NFW dictionary. The penalization parameters are  $\lambda = 3.5$  (left) and  $\lambda = 5.0$  (right). The input halo mass is  $M_{200} = 10^{15.02} h^{-1} M_{\odot}$ , and its redshift is  $z = 0.164$ . The vertical direction is the line of sight direction. The boxes' lower boundaries and upper boundaries of correspond to  $z = 0.01$  and  $z = 0.85$ , respectively.

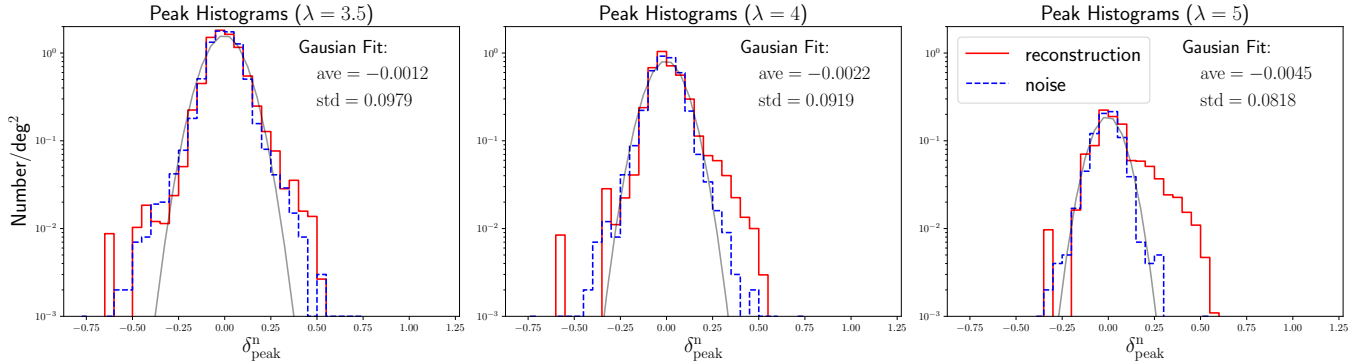


**Figure 10.** The number per square degree histograms of detected peak values from all of the simulations. The solid red steps result from reconstructions with the NFW dictionary penalized with different regularization parameters:  $\lambda = 3.5, 4.0, 5.0$ . The dashed blue steps are the corresponding results of the reconstructions from 1000 realizations of pure noise catalogs. The gray lines are the best-fit Gaussian distributions to the noises' peak histograms.

We select peaks with values greater than an ad-hoc threshold as candidates of galaxy clusters following Miyazaki et al. (2018). The threshold is set to a few times the standard deviation of the noise peaks. We use different detection thresholds ( $1.5\sigma$  and  $3.0\sigma$ ) to detect galaxy clusters from the mass maps reconstructed with  $\lambda = 3.5, 4.0, 5.0$ . The left and middle columns of Figure 12 show the detection rates for halos in the (mass, redshift) planes with detection thresholds set to  $1.5\sigma$  and  $3.0\sigma$  of the noise peaks' distributions, respectively. The right column of Figure 12 shows the corresponding numbers of false detections per square degree as functions of detection thresholds. The first, second, and third rows of Figure 12 correspond to the  $\lambda = 3.5, 4.0, 5.0$ , respectively.

Figure 12 tells that the false peak density is suppressed as the detection threshold increases. Also, the detection rate of halo significantly decreases. We decide to set the detection threshold to  $1.5\sigma$  and set the penalization parameter  $\lambda$  to 5.0 since such a setup suppresses the false

detection to 0.022 while keeping a good halo detection rate. In summary, The algorithm is able to detect halo with minimal mass limits of  $10^{14.0} M_{\odot}/h$ ,  $10^{14.7} M_{\odot}/h$ ,  $10^{15.0} M_{\odot}/h$  for the low ( $z < 0.3$ ), median ( $0.3 \leq z < 0.6$ ) and high ( $0.6 \leq z < 0.85$ ) redshifts, respectively.

### 3.3. Point mass atoms

We substitute the default NFW dictionary with the point mass dictionary and reconstruct the mass map from the mock galaxy shape catalog, to compare with the default setup.

The regularization parameter ( $\lambda$ ) for the preliminary lasso is set to 3.5 and 5.0. Inspired by Pramanik & Zhang (2020), which propose to incorporate external group information into different adaptive lasso penalization weights by setting the penalization weights for projection coefficients in the same group to the average of the adaptive weights in this group, we smooth the preliminary lasso estimation in each lens redshift bin with a top-hat filter of comoving scale  $0.25 h^{-1}$

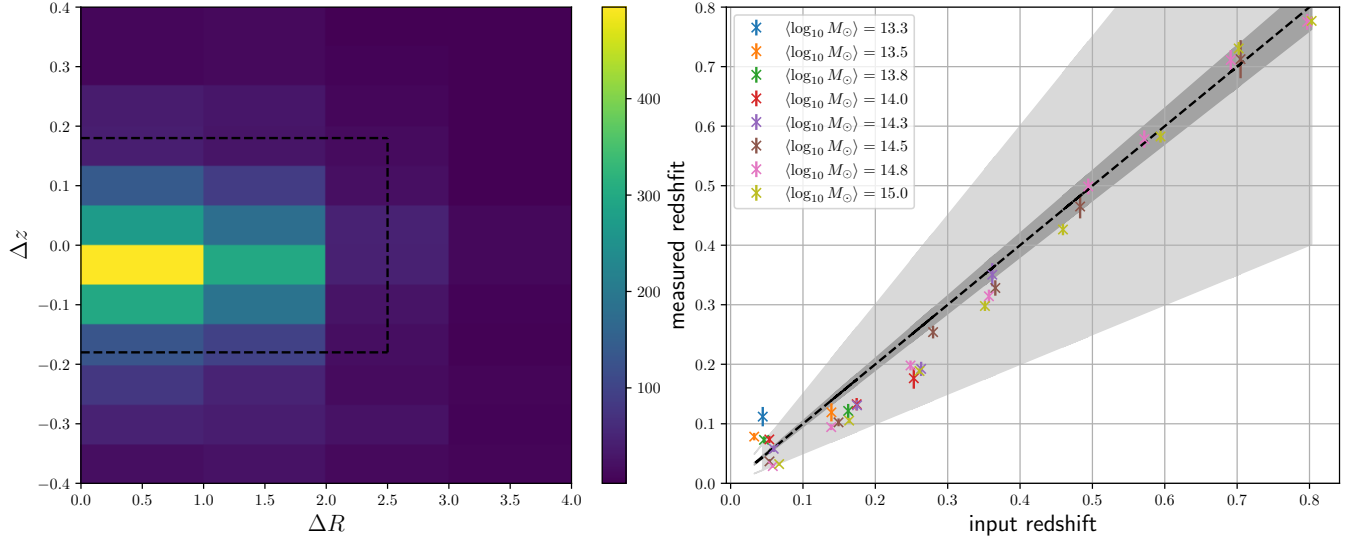


**Figure 11.** The left panel shows the stacked 2-D distribution of the deviations of detected peak positions from the centers of the corresponding input halos. The  $x$ -axis is for the deviated distance in the transverse plane, and the  $y$ -axis is for the deviation of the redshift. For each simulation, the positive peak inside the dashed black box with the minimal offset (in the pixel unit) from the input halo’s position is taken as a true detection. The right panel focuses on the deviation of detected peaks in the line of sight direction. The  $x$ -axis is the input halo redshifts, and the  $y$ -axis is the redshift of the detected peak. The ‘ $\times$ ’ denotes the average redshift of detected peaks for each halo over different noise realizations, and the error-bars are the uncertainties of the average redshifts. The deep gray area is for the relative redshift bias less than 0.05, and the light gray area is for the relative redshift bias less than 0.5. These results in this figure are based on the NFW dictionary with  $\lambda = 3.5$ .

Mpc. The smoothed preliminary lasso estimation is denoted as  $\hat{x}_{\text{sm}}^{\text{ls}}$ , and the penalization weights are set to  $\hat{w} = 1/|\hat{x}_{\text{sm}}^{\text{ls}}|^{\tau}$ . The regularization parameter for the adaptive lasso is set to  $\lambda_{\text{ada}} = \lambda$ . As we have done on the NFW dictionary’s reconstruction, we smooth the reconstructed density maps with the Gaussian kernel (scale radius equals 1.5) in each lens redshift plane.

As demonstrated in Figure 13, the mass reconstructions with the point mass dictionary tend to assign masses to several different redshift bins in the neighboring region of the halo’s center. In contrast, as demonstrated in Figure 9, the NFW dictionary manages to perform consistent mass reconstructions. We think the problem of the point mass dictionary originates from the fact that the profile of the point mass atom in the transverse plane is much more compact than the profile of the input halos, especially at low redshift.

#### 4. SUMMARY

We develop a novel method to reconstruct 3-D density contrast maps from weak-lensing shear measurements and photometric redshift estimations. Our method models 3-D density contrast maps as summations of NFW atoms with different comoving radii. With the prior assumption that the clumpy masses sparsely distribute in the 3-D space, the density map is reconstructed using the adaptive lasso algorithm (Zou 2006).

The method is tested with realistic simulations using HSC-like shape estimation errors and photo- $z$  uncertainties.

The findings of this paper are summarized as follows:

(i) The lasso algorithm’s solution suffers from a smear of structure in the line of sight direction even in the absence of shape noise, and the adaptive lasso algorithm significantly removes the line of sight smear of structure.

(ii) The algorithm is able to detect halo with minimal mass limits of  $10^{14.0}M_{\odot}/h$ ,  $10^{14.7}M_{\odot}/h$ ,  $10^{15.0}M_{\odot}/h$  for the low ( $z < 0.3$ ), median ( $0.3 \leq z < 0.6$ ) and high ( $0.6 \leq z < 0.85$ ) redshifts, respectively, with a false detection of 0.022/deg<sup>2</sup>.

(iii) The estimated redshifts of the halos detected from the reconstructed mass maps are lower than the true redshift by about 0.03 for halos at low redshifts ( $z \leq 0.4$ ). The relative redshift bias is below 0.5% for halos at  $0.4 < z \leq 0.85$ .

We will apply the method to the shear measurements of the HSC survey (Mandelbaum et al. 2018; Li et al. 2020) to perform galaxy cluster detection in our future work.

#### ACKNOWLEDGEMENTS

XL thank Yin Li and Jiaxin Han for useful discussions.

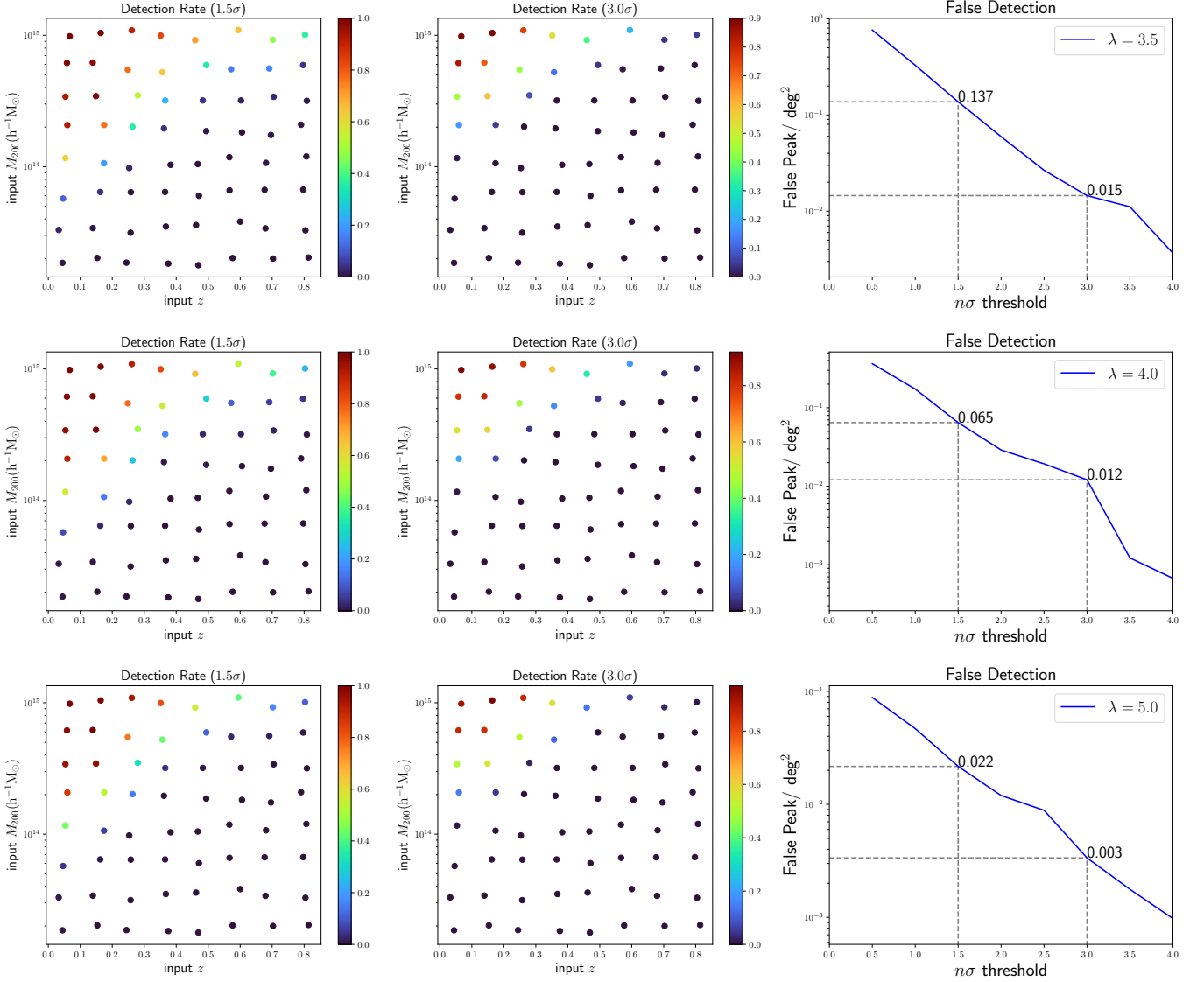


**Figure 12.** The detection rates and false peak densities for different penalization parameters and detection thresholds. The first, second, and third rows correspond to the results with  $\lambda = 3.5, 4.0, 5.0$ , respectively. The left and middle columns are the halo detection rates for detection thresholds equal  $1.5\sigma$  and  $3.0\sigma$ , respectively. The right column shows the density of false peaks as a function of detection threshold.

XL was supported by Global Science Graduate Course (GSGC) program of University of Tokyo and JSPS KAKENHI (JP19J22222).

## REFERENCES

- Aihara, H., Armstrong, R., Bickerton, S., et al. 2018, PASJ, 70, S8, doi: [10.1093/pasj/psx081](https://doi.org/10.1093/pasj/psx081)
- Beck, A., & Teboulle, M. 2009, SIAM Journal on Imaging Sciences, 2, 183
- Carrasco Kind, M., & Brunner, R. J. 2013, MNRAS, 432, 1483, doi: [10.1093/mnras/stt574](https://doi.org/10.1093/mnras/stt574)
- Chang, C., Pujol, A., Mawdsley, B., et al. 2018, MNRAS, 475, 3165, doi: [10.1093/mnras/stx3363](https://doi.org/10.1093/mnras/stx3363)
- de Jong, J. T. A., Verdoes Kleijn, G. A., Kuijken, K. H., & Valentijn, E. A. 2013, Experimental Astronomy, 35, 25, doi: [10.1007/s10686-012-9306-1](https://doi.org/10.1007/s10686-012-9306-1)
- Hamana, T., Shirasaki, M., Miyazaki, S., et al. 2020, PASJ, 72, 16, doi: [10.1093/pasj/psz138](https://doi.org/10.1093/pasj/psz138)

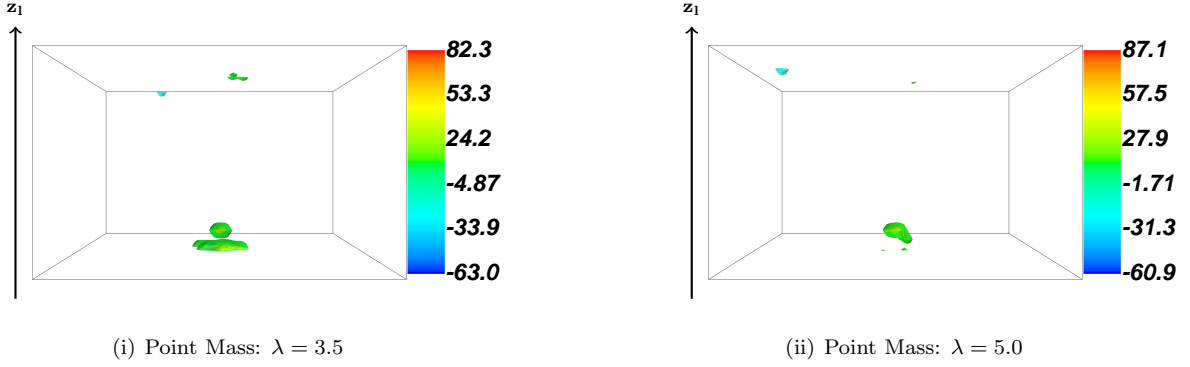


**Figure 13.** The density maps reconstructed from the mock galaxy shape catalog with the point mass dictionary. The penalization parameters are  $\lambda = 3.5$  (left) and  $\lambda = 5.0$  (right). The input halo mass is  $M_{200} = 10^{15.02} h^{-1} M_{\odot}$ , and its redshift is  $z = 0.164$ . The vertical direction is the line of sight direction. The boxes' lower boundaries and upper boundaries of correspond to  $z = 0.01$  and  $z = 0.85$ , respectively.

- Han, J., Eke, V. R., Frenk, C. S., et al. 2015, MNRAS, 446, 1356, doi: [10.1093/mnras/stu2178](https://doi.org/10.1093/mnras/stu2178)
- Hikage, C., Oguri, M., Hamana, T., et al. 2019, PASJ, 71, 43, doi: [10.1093/pasj/psx010](https://doi.org/10.1093/pasj/psx010)
- Hildebrandt, H., Köhlinger, F., van den Busch, J. L., et al. 2020, ap, 633, A69, doi: [10.1051/0004-6361/201834878](https://doi.org/10.1051/0004-6361/201834878)
- Jeffrey, N., Abdalla, F. B., Lahav, O., et al. 2018, MNRAS, 479, 2871, doi: [10.1093/mnras/sty1252](https://doi.org/10.1093/mnras/sty1252)
- Kaiser, N., & Squires, G. 1993, pj, 404, 441, doi: [10.1086/172297](https://doi.org/10.1086/172297)
- Kilbinger, M. 2015, Reports on Progress in Physics, 78, 086901, doi: [10.1088/0034-4885/78/8/086901](https://doi.org/10.1088/0034-4885/78/8/086901)
- Lanusse, F., Starck, J. L., Leonard, A., & Pires, S. 2016, ap, 591, A2, doi: [10.1051/0004-6361/201628278](https://doi.org/10.1051/0004-6361/201628278)
- Laureijs, R., Amiaux, J., Arduini, S., et al. 2011, ArXiv e-prints. <https://arxiv.org/abs/1110.3193>
- Leonard, A., Lanusse, F., & Starck, J.-L. 2014, MNRAS, 440, 1281, doi: [10.1093/mnras/stu273](https://doi.org/10.1093/mnras/stu273)
- Li, X., Oguri, M., Katayama, N., et al. 2020, The Astrophysical Journal Supplement Series, 251, 19, doi: [10.3847/1538-4365/abbad1](https://doi.org/10.3847/1538-4365/abbad1)
- LSST Science Collaboration, Abell, P. A., Allison, J., et al. 2009, ArXiv e-prints. <https://arxiv.org/abs/0912.0201>
- Mandelbaum, R. 2018, ARA&A, 56, 393, doi: [10.1146/annurev-astro-081817-051928](https://doi.org/10.1146/annurev-astro-081817-051928)
- Mandelbaum, R., Miyatake, H., Hamana, T., et al. 2018, PASJ, 70, S25, doi: [10.1093/pasj/psx130](https://doi.org/10.1093/pasj/psx130)
- Miyazaki, S., Oguri, M., Hamana, T., et al. 2018, PASJ, 70, S27, doi: [10.1093/pasj/psx120](https://doi.org/10.1093/pasj/psx120)
- More, S., Miyatake, H., Mandelbaum, R., et al. 2015, The Astrophysical Journal, 806, 2, doi: [10.1088/0004-637x/806/1/2](https://doi.org/10.1088/0004-637x/806/1/2)
- Morrison, C. B., Klaes, D., van den Busch, J. L., et al. 2016, Monthly Notices of the Royal Astronomical Society, 465, 1454, doi: [10.1093/mnras/stw2805](https://doi.org/10.1093/mnras/stw2805)
- Navarro, J. F., Frenk, C. S., & White, S. D. M. 1997, pj, 490, 493, doi: [10.1086/304888](https://doi.org/10.1086/304888)
- Oguri, M., Miyazaki, S., Hikage, C., et al. 2018, PASJ, 70, S26, doi: [10.1093/pasj/psx070](https://doi.org/10.1093/pasj/psx070)
- Planck Collaboration, Aghanim, N., Akrami, Y., et al. 2020, ap, 641, A6, doi: [10.1051/0004-6361/201833910](https://doi.org/10.1051/0004-6361/201833910)
- Pramanik, S., & Zhang, X. 2020, arXiv e-prints, arXiv:2006.02041. <https://arxiv.org/abs/2006.02041>
- Prat, J., Sánchez, C., Fang, Y., et al. 2018, Phys. Rev. D, 98, 042005, doi: [10.1103/PhysRevD.98.042005](https://doi.org/10.1103/PhysRevD.98.042005)
- Price, M. A., Cai, X., McEwen, J. D., et al. 2020, MNRAS, 492, 394, doi: [10.1093/mnras/stz3453](https://doi.org/10.1093/mnras/stz3453)
- Ragagnin, A., Dolag, K., Moscardini, L., Biviano, A., & D'Onofrio, M. 2019, MNRAS, 486, 4001, doi: [10.1093/mnras/stz1103](https://doi.org/10.1093/mnras/stz1103)
- Simon, P., Taylor, A. N., & Hartlap, J. 2009, MNRAS, 399, 48, doi: [10.1111/j.1365-2966.2009.15246.x](https://doi.org/10.1111/j.1365-2966.2009.15246.x)
- Spergel, D., Gehrels, N., Baltay, C., et al. 2015, ArXiv e-prints. <https://arxiv.org/abs/1503.03757>
- Starck, J., Murtagh, F., & Bertero, M. 2015, Starlet transform in astronomical data processing, Vol. 1 (United States: Springer New York), 2053–2098
- Takada, M., & Jain, B. 2003, MNRAS, 340, 580, doi: [10.1046/j.1365-8711.2003.06321.x](https://doi.org/10.1046/j.1365-8711.2003.06321.x)
- Tanaka, M., Coupon, J., Hsieh, B.-C., et al. 2018, Publications of the Astronomical Society of Japan, 70, S9, doi: [10.1093/pasj/psx077](https://doi.org/10.1093/pasj/psx077)
- The Dark Energy Survey Collaboration. 2005, ArXiv Astrophysics e-prints
- Troxel, M. A., MacCrann, N., Zuntz, J., et al. 2018, Phys. Rev. D, 98, 043528, doi: [10.1103/PhysRevD.98.043528](https://doi.org/10.1103/PhysRevD.98.043528)
- Zou, H. 2006, Journal of the American Statistical Association, 101, 1418, doi: [10.1198/016214506000000735](https://doi.org/10.1198/016214506000000735)